

Supporting information for

# Single-Atom Oxygen Reduction Reaction Electrocatalysts of Fe, Si, and N co-doped Carbon with 3D Interconnected Mesoporosity

*Hee Soo Kim<sup>a, #</sup>, Chi Ho Lee<sup>b, #</sup>, Jue-Hyuk Jang<sup>a, #</sup>, Min Seok Kang<sup>c</sup>, Haneul Jin<sup>a</sup>, Kug-Seung Lee<sup>d</sup>, Sang Uck Lee<sup>e,f\*</sup>, Sung Jong Yoo<sup>a, g, h \*</sup>, and Won Cheol Yoo<sup>e,f\*</sup>*

<sup>a</sup>Center for Hydrogen-Fuel Cell Research, Korea Institute of Science and Technology (KIST), Seoul 02792, Republic of Korea.

<sup>b</sup>Department of Bionano Technology, Hanyang University, Ansan, 15588, Republic of Korea.

<sup>c</sup>Department of Applied Chemistry, Hanyang University, Ansan, 15588, Republic of Korea.

<sup>d</sup>Pohang Accelerator Laboratory, 80 Jigokro-123-beongil, Nam-gu, Pohang, Gyeongbuk 37673, Republic of Korea.

<sup>e</sup>Department of Chemical and Molecular Engineering, Hanyang University, 55 Hanyangdaehak-ro, Sangnok-gu, Ansan, 15588, Republic of Korea.

<sup>f</sup>Department of Applied Chemistry, Center for Bionano Intelligence Education and Research, Hanyang University, Ansan, 15588, Republic of Korea.

<sup>g</sup>KHU-KIST Department of Converging Science and Technology, Kyung Hee University, Seoul 02447, Republic of Korea.

<sup>h</sup>Division of Energy & Environment Technology, KIST School, University of Science and Technology (UST), Seoul, 02792, Republic of Korea

## Author information

<sup>#</sup> These authors contributed equally to this work

## Corresponding Author

\*E-mail: sulee@hanyang.ac.kr (S. U. Lee)

\*E-mail: ysj@kist.re.kr (S. J. Yoo)

\*E-mail: wcyoo@hanyang.ac.kr (W. C. Yoo)

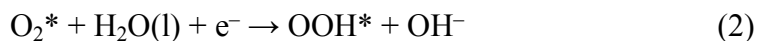
## Theoretical Methods

### Computational Details and Modeling

All *ab initio* calculations were performed with the Vienna *Ab initio* Simulation Package (VASP 5.4.4)<sup>S1-S5</sup>. We used the BEEF-vdW<sup>S6</sup> exchange-correlation functional using the projector augmented wave (PAW) method<sup>S6,S7</sup> with a generalized gradient to accurately describe the chemisorption as well as physisorption on the catalytic surface. Integration in the Brillouin zone was performed based on the Monkhorst-Pack scheme using a  $\Gamma$ -centered  $2 \times 2 \times 1$  k-point mesh in each primitive lattice vector of the reciprocal space for geometric optimization. A plane-wave cutoff energy of 500 eV was used. Lattice constants and internal atomic positions were fully optimized until the residual forces were less than 0.04 eV/ Å. The vacuum slab space of a unit cell in the z-direction was set to 20 Å to avoid interactions between layers. The schematics of our models are shown as Supplementary Figure S8 and S10. For the convenience of identifying the active site positions, we name them by element name and Arabic number. The details of the active site naming are also included in Supplementary Figure S8 and S10.

### ORR Reaction Pathways

In this work, we used the theoretically well-defined free energy diagram (FED) approach proposed by Norskov group. It has been generally accepted method for the electrochemical activity works based on density functional calculations, in which the thermodynamic stabilities of the intermediates for catalytic reactions can be used as the main descriptor on the catalytic activity<sup>S8,S9</sup>. In the oxygen reduction reaction (ORR), we considered the overall reaction mechanism for the complete direct four-electron process, in which O<sub>2</sub> is reduced to water without the formation of the hydrogen peroxide intermediate, H<sub>2</sub>O<sub>2</sub>. Also, this mechanism in an alkaline environment can be described as follows:





, where \* represents the active site, and  $O_2^*$ ,  $OOH^*$ ,  $O^*$  and  $OH^*$  are adsorbed intermediates on the surface.

### Derivation of the free energy relations

We calculated the reaction Gibbs free energies of the intermediates  $O_2^*$ ,  $OOH^*$ ,  $O^*$  and  $OH^*$  on the pure and Si doped FNC structures with six different structural conformations (BP1, BP2, AE, ZE, IE1, and IE2, where BP, AE, ZE and IE represent basal plane, armchair edge, zigzag edge and inter-edge, respectively.) to determine the point of the potential-determining step of ORR on various reaction sites for different structure. For each step, the reaction Gibbs free energy  $\Delta G_{ads}$  can be expressed by,

$$\Delta G_{ads} = \Delta E_{ads} + \Delta ZPE - T\Delta S \quad (6)$$

where ZPE is the zero-point energy, T is the temperature, and  $\Delta S$  is the entropy change. Using this equation (S10), we can construct free energy diagram (FED) considering the following four electrons/four steps with equations at standard conditions<sup>S10</sup>.

The reaction Gibbs free energy of each electrochemical reaction of ORR in alkaline media can be expressed as follows:

$$\Delta G_1 = (G_{OOH^*} + \mu_{OH^-}) - (G_* + \mu_{O2} + \mu_{H2O(l)} + \mu_{e^-}) \quad (7)$$

$$\Delta G_2 = (G_{O^*} + \mu_{OH^-}) - (G_{OOH^*} + \mu_{e^-}) \quad (8)$$

$$\Delta G_3 = (G_{OH^*} + G_*) - (G_{O^*} + \mu_{H2O(l)} + \mu_{e^-}) \quad (9)$$

$$\Delta G_4 = (\mu_{OH^-} + G_*) - (G_{OH^*} + \mu_{e^-}) \quad (10)$$

These free energy change values can be calculated by using the chemical potentials of hydroxide, electron, liquid water, and oxygen molecule ( $\mu_{OH^-}$ ,  $\mu_{e^-}$ ,  $\mu_{H2O(l)}$  and  $\mu_{O2}$ ) and the free energies of each intermediates ( $G_{OH^*}$ ,  $G_*$ ,  $G_{OOH^*}$ ) on the surface (\*).

### Free energy diagram (FED) and Overpotential ( $\eta$ )

From the calculated  $\Delta G$  values, we can deduce a critical parameter of electrocatalytic activity, which is the magnitude of the ORR potential-determining step ( $G^{ORR}$ ) in four electrons/four steps. It is the specific reaction point with the largest  $\Delta G$  in the ORR elementary reaction steps; i.e., the concluding step to achieve a downhill reaction in the free energy diagram (FED) with increasing potential (Supplementary Figure S12 and S13):

$$G^{ORR} = \max[\Delta G_1, \Delta G_2, \Delta G_3, \Delta G_4]^0 \quad (11)$$

After finding the largest  $\Delta G$  value meaning bottleneck point of ORR, we can finally get the theoretical overpotential in alkaline condition in the following equation (12):

$$\eta^{ORR} = (G^{ORR}/e) - xV, x = 0.402 \text{ V} \quad (12)$$

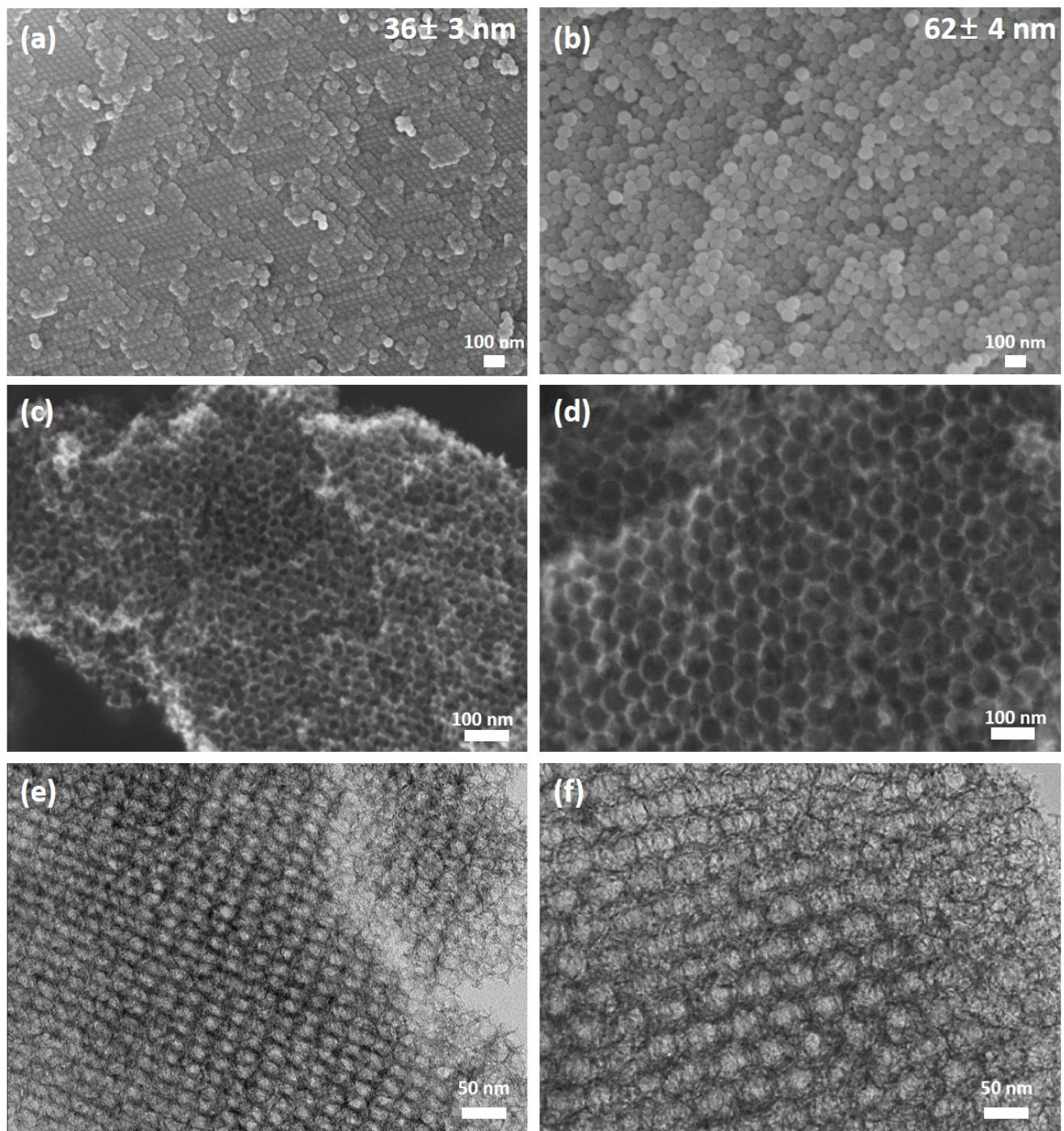


**Fig S1.** SEM images of  $36 \pm 3$  and  $62 \pm 4$  nm closed packed  $\text{SiO}_2$  (a and b). SEM and TEM images of 3DMC\_25 (c,e) and 3DMC\_50 (e,f).

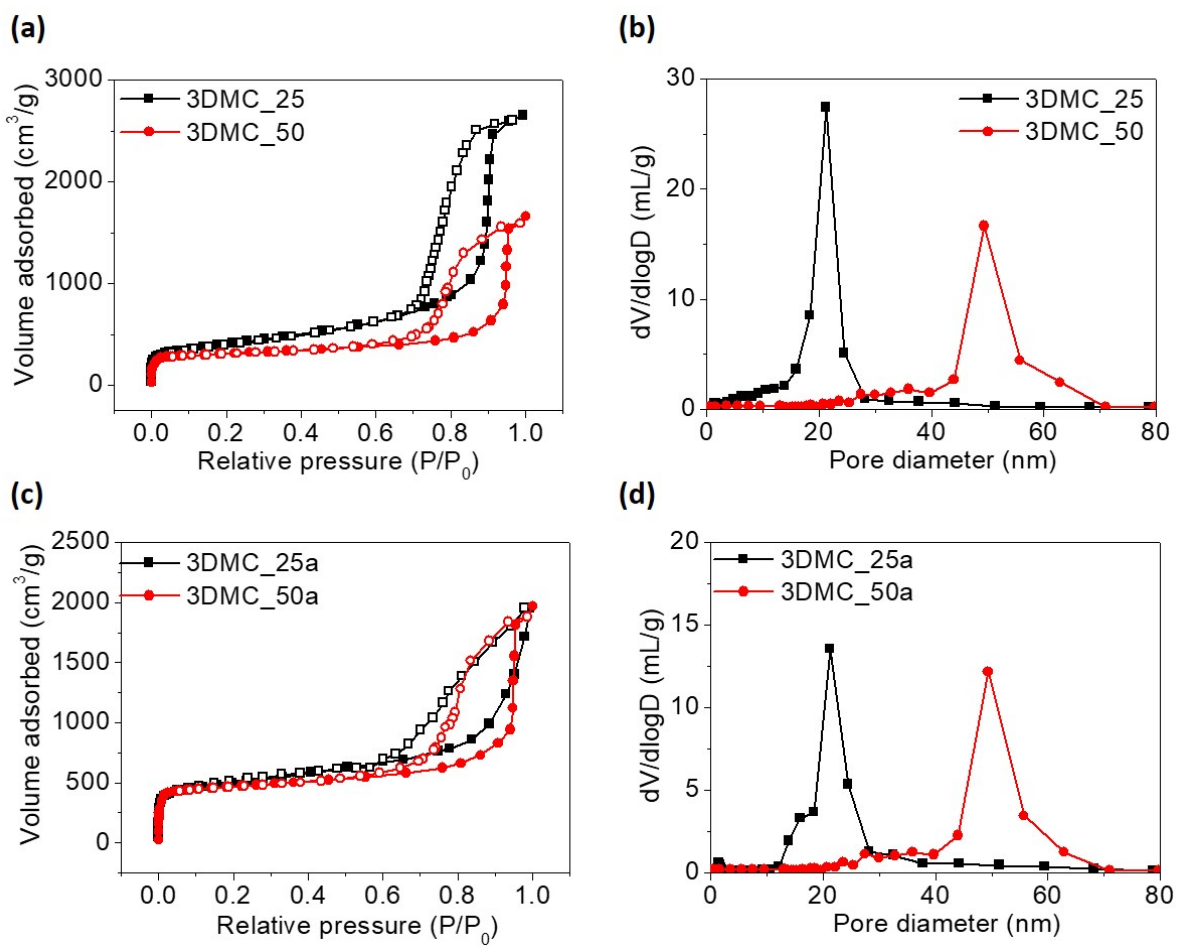


**Fig S2.** N<sub>2</sub> sorption isotherms (a and c) and BJH profiles (b and d) of 3DMC\_25 and 50 samples.

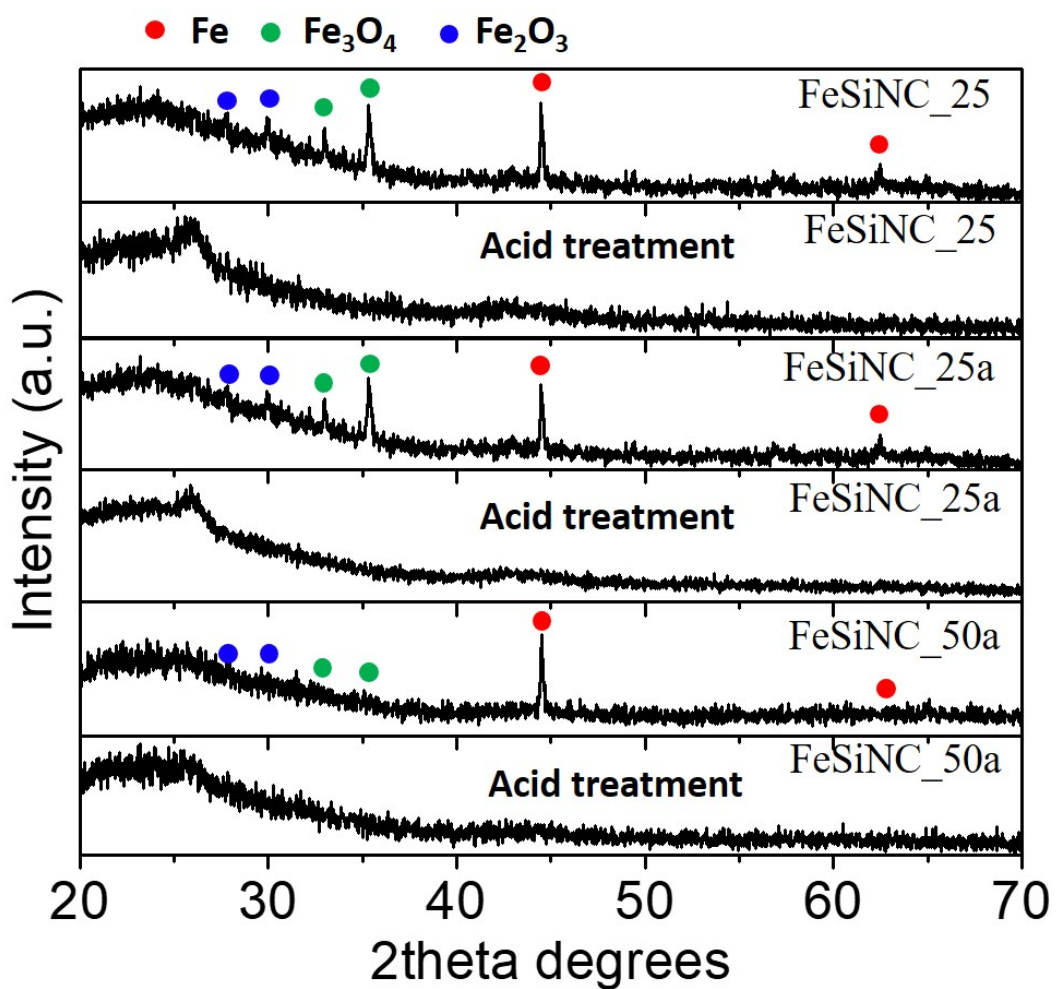


**Fig S3.** XRD results of FeSiNC samples before and after acid treatment.

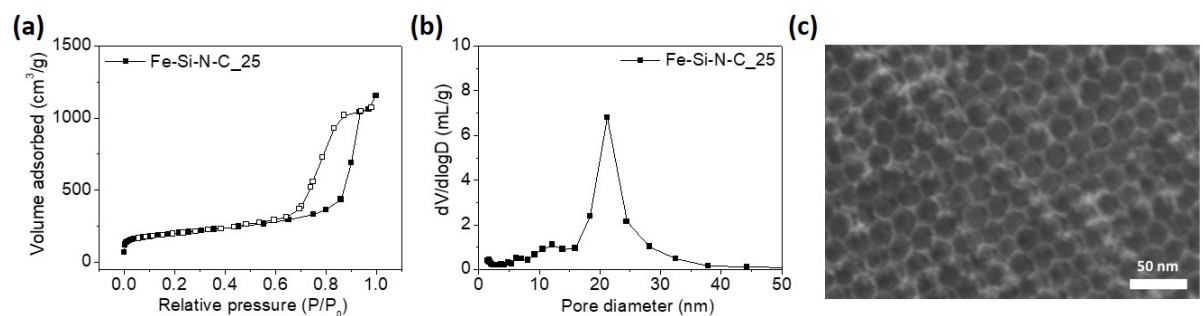


**Fig S4.**  $\text{N}_2$  sorption (a), BJH plot of (b), and SEM image (c) of FeSiNC\_25.

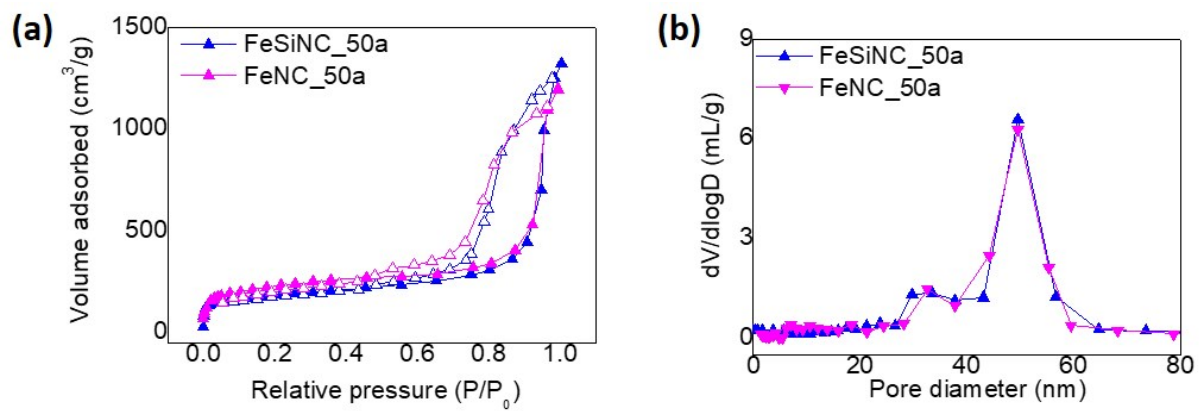


**Fig S5.** N<sub>2</sub> sorption isotherms (a) and BJH plots (b) of FeSiNC\_50a and FeNC\_50a.

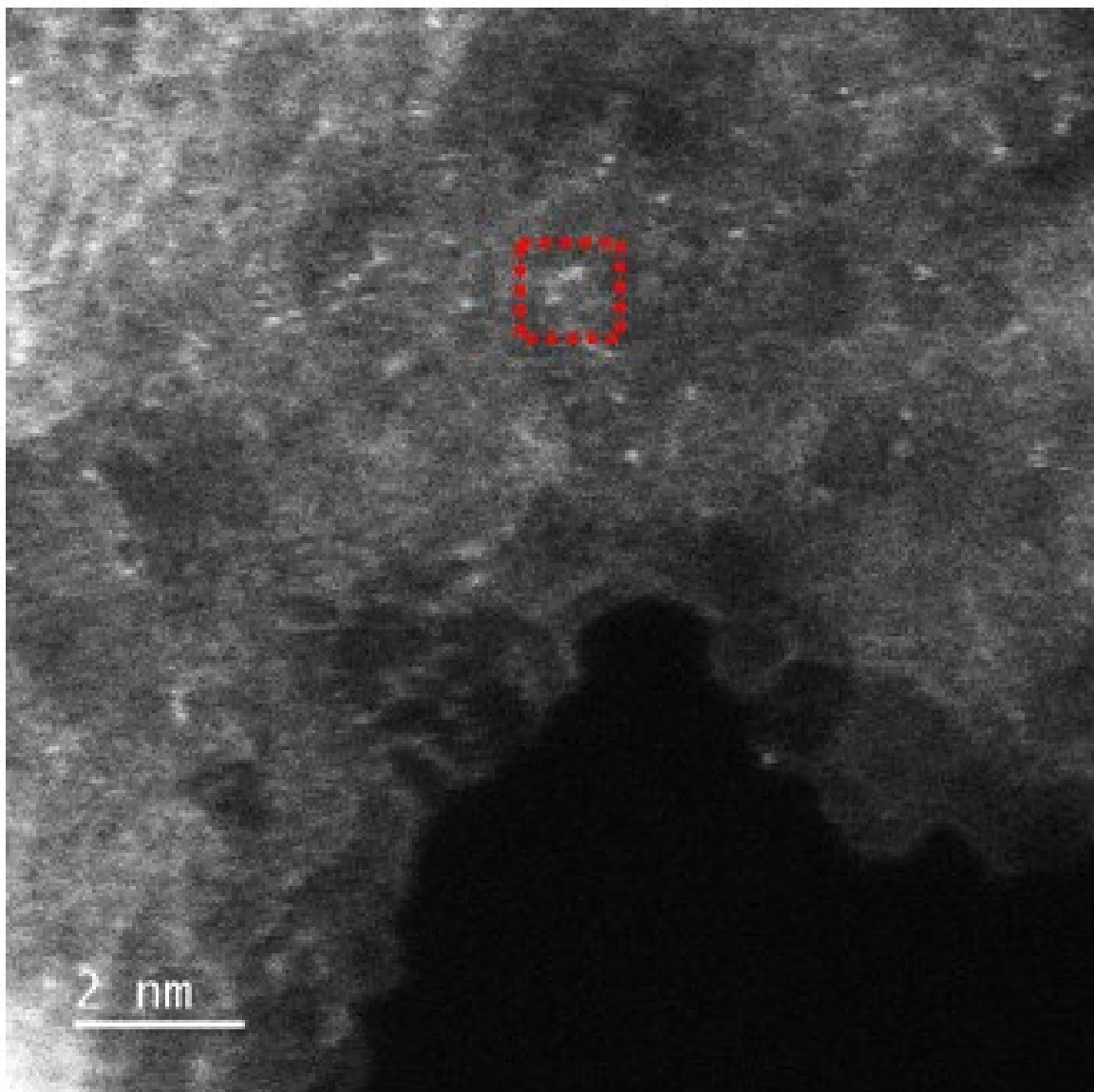


**Fig S6.** HAADF image of FeSiNC\_50a: EEL spectra displayed in Fig 2C was obtained from the red square area.

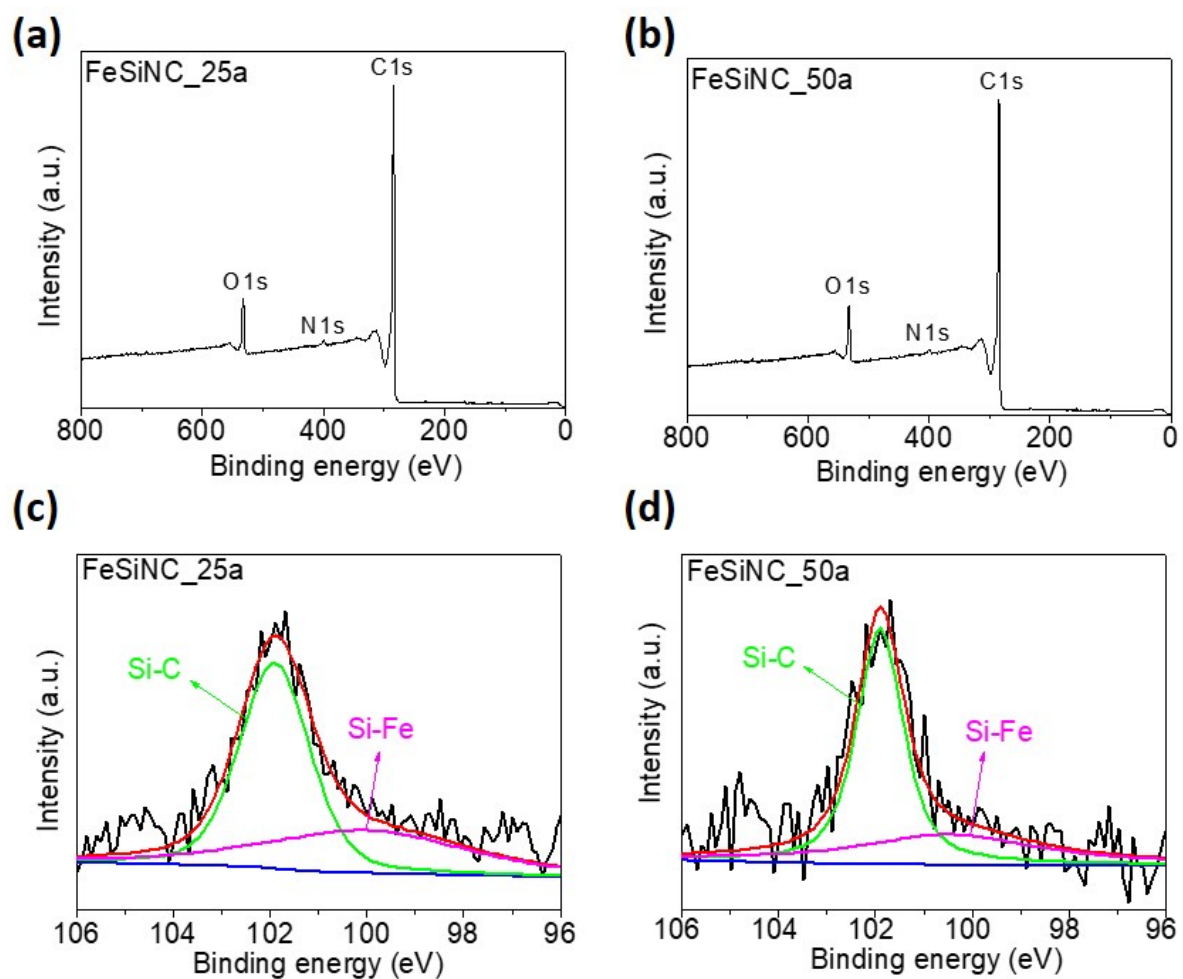


**Fig S7.** XPS survey spectra (a-b) and high-resolution XPS spectra (c-d) of Si 2p of FeSiNC\_25a and 50a samples.

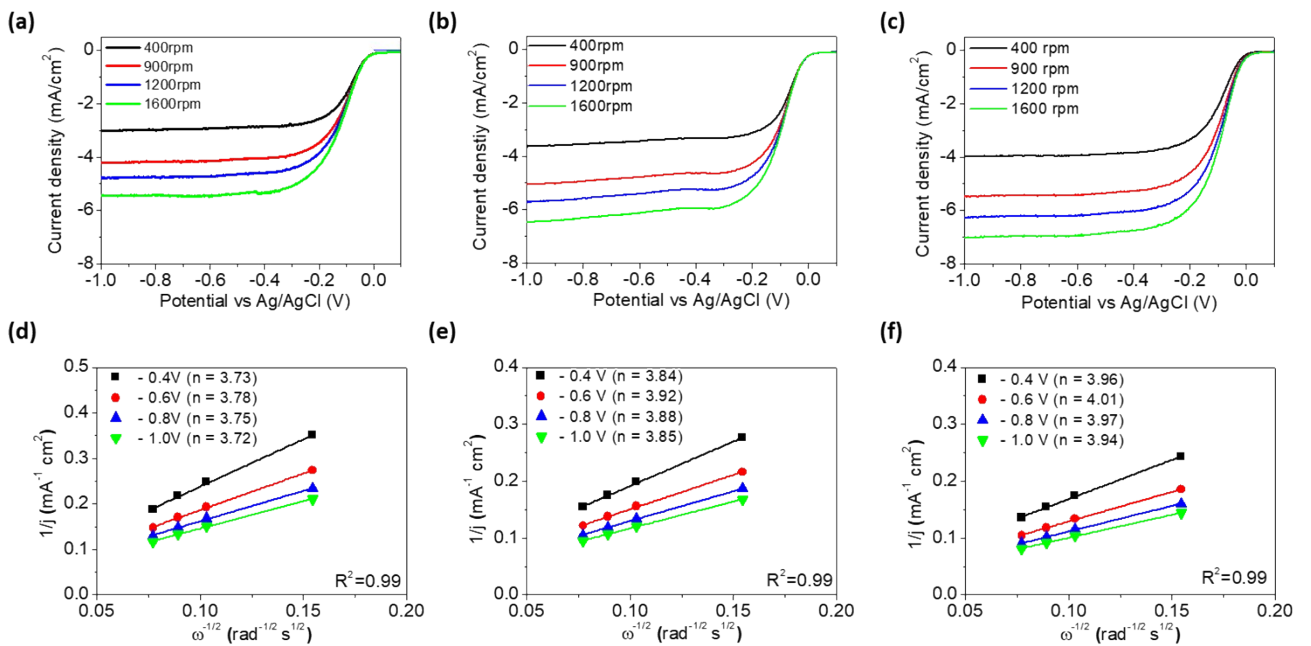


**Fig S8.** LSV curves of FeSiNC\_25 (a), FeSiNC\_25a (b), and FeSiNC\_50a (c) from 400 to 1600 rpm (0.1M KOH) and Koutecky-Levich (K-L) plots at various voltages of FeSiNC\_25 (d), FeSiNC\_25a (e), and FeSiNC\_50a (f).

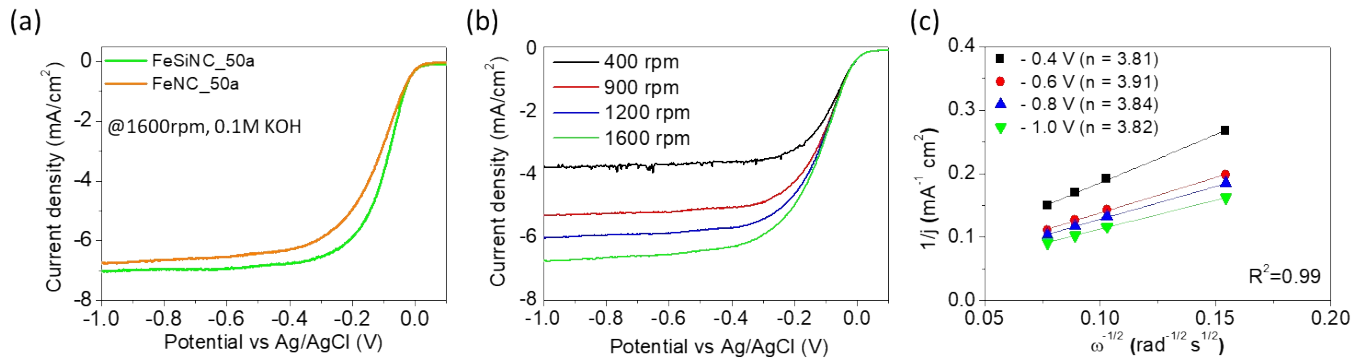


**Fig S9.** Comparison of polarization curves for FeSiNC\_50a and FeNC\_50a at 1600 rpm (a), polarization curves from 400 to 1600 rpm for FeNC\_50a (b), and K-L plots at various voltages (c) for FeNC\_50a.

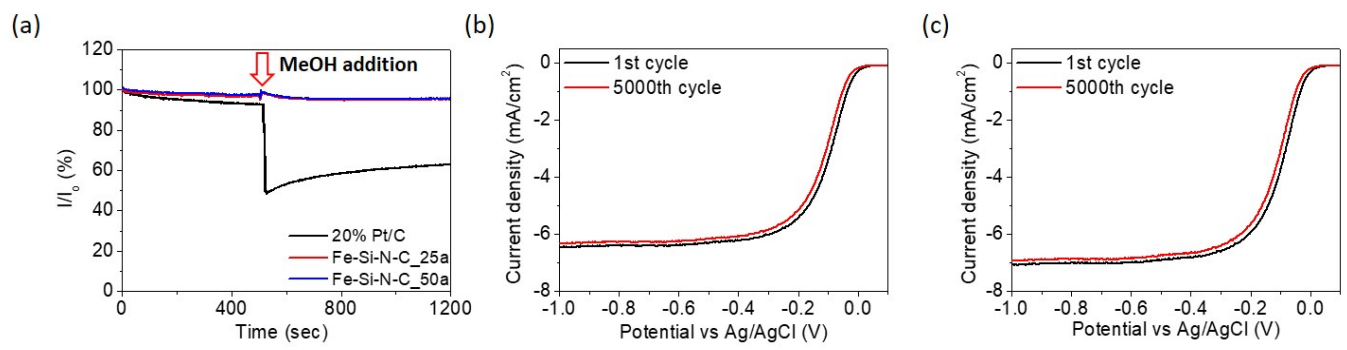


**Fig S10.** Chronoamperometric responses (a) at -0.4 V vs Ag/AgCl (V) with injection of methanol at 500 sec. The ORR polarization curves of FeSiNC\_25a (b) and FeSiNC\_50a (c) in O<sub>2</sub>-saturated 0.1 M KOH solution before and after 5000 potential cycles between 0 to -0.4 V vs Ag/AgCl (V).

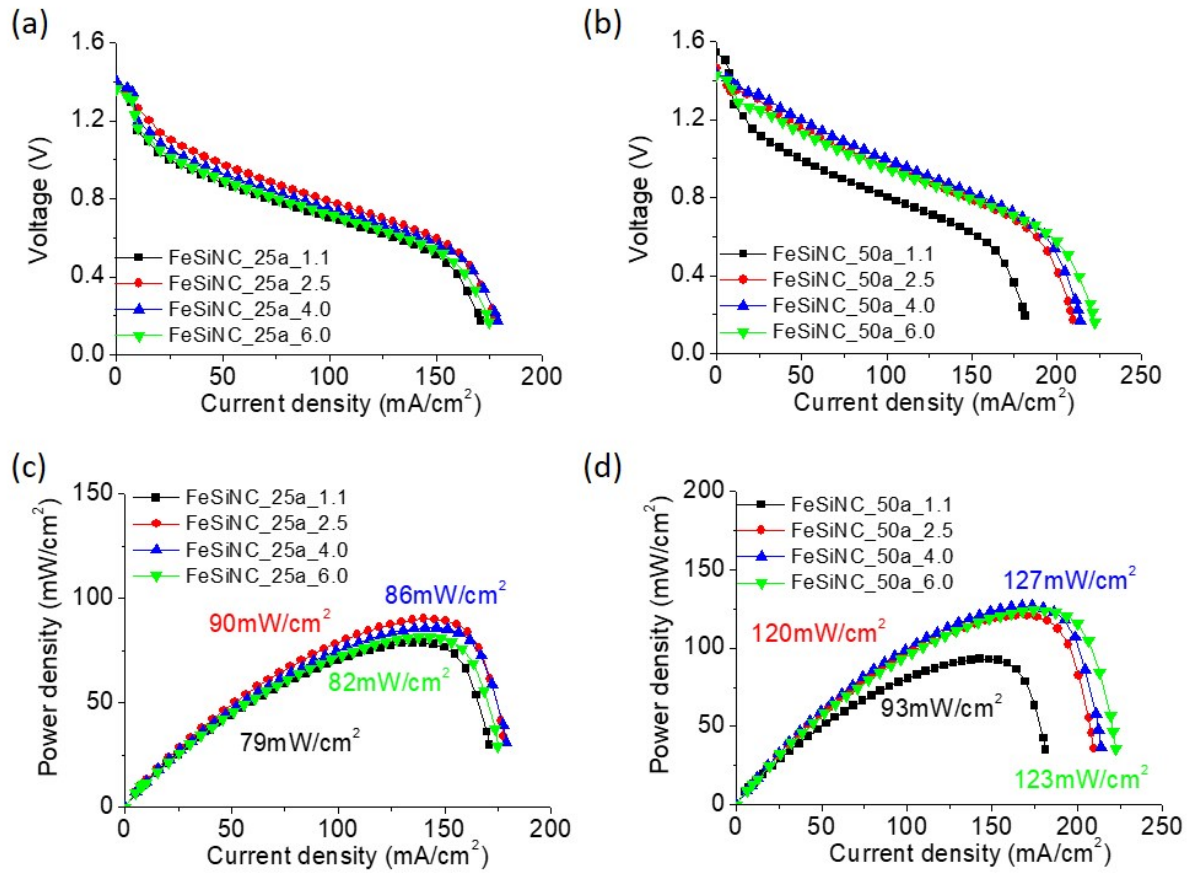


**Fig S11.** Polarization curves and power density plots of FeSiNC\_25a (a and c), and FeSiNC\_50a (b and d).

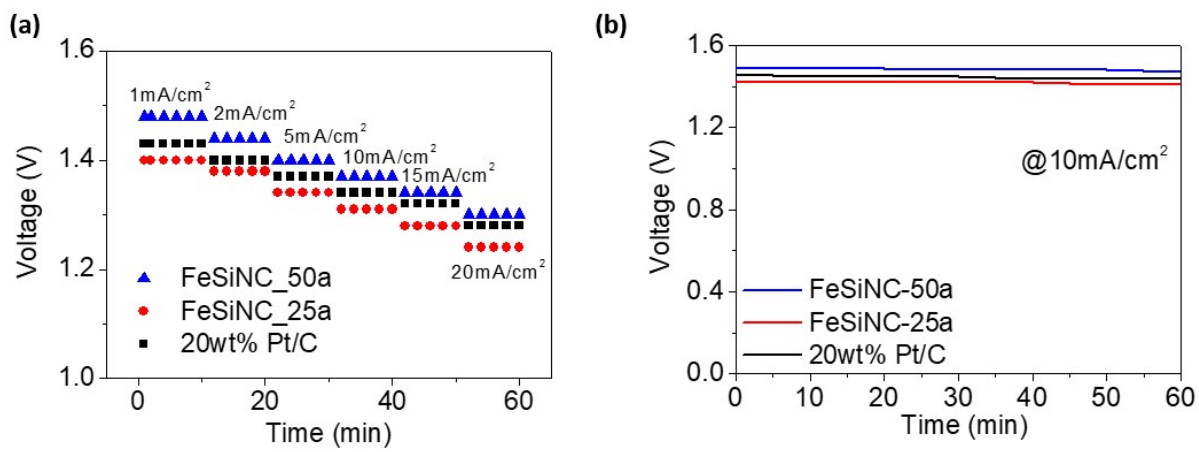


**Fig S12.** The rate performances (a) and galvanostatic discharge curves of FeSiNC\_25a and 50 and the commercial Pt/C at catalyst loading of 2.5 mg/cm<sup>2</sup>.

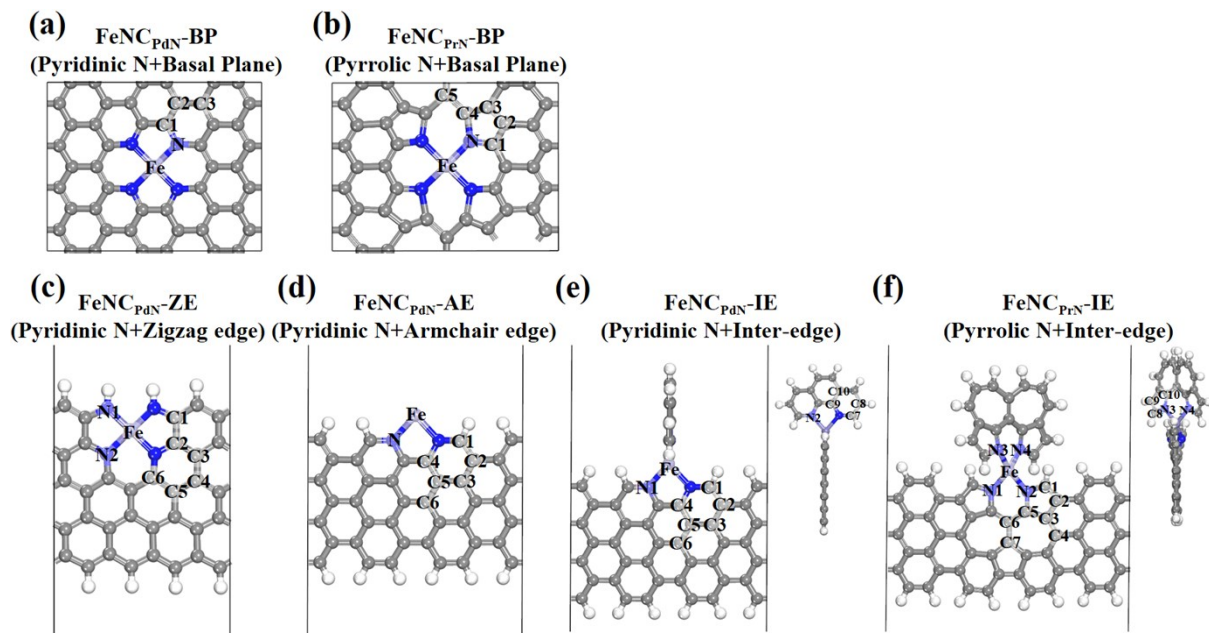


**Fig S13.** Possible Fe and N co-doped graphene structures (FeNCs) of (a)  $\text{FeNC}_{\text{PdN}}\text{-BP}$ , (b)  $\text{FeNC}_{\text{PrN}}\text{-BP}$ , (c)  $\text{FeNC}_{\text{PdN}}\text{-ZE}$ , (d)  $\text{FeNC}_{\text{PdN}}\text{-AE}$ , (e)  $\text{FeNC}_{\text{PdN}}\text{-IE}$  and (f)  $\text{FeNC}_{\text{PrN}}\text{-IE}$  ( $\text{PdN/PrN}$  and  $\text{BP/AE/ZE/IE}$  represent pyridinic/pyrrolic N, and basal plane/armchair/zigzag/inter-edge, respectively).

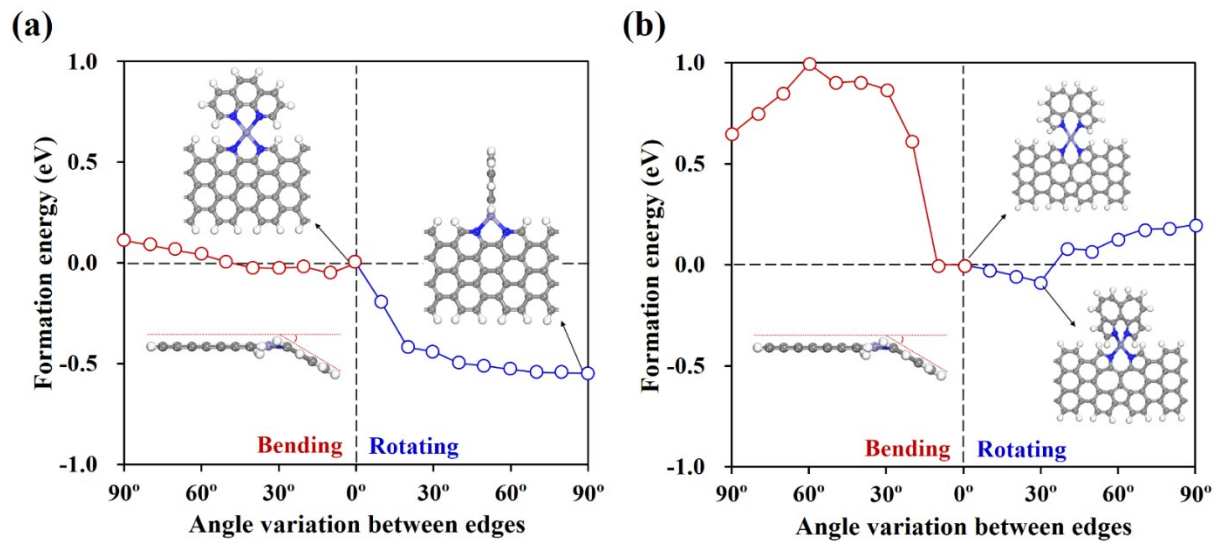


**Fig S14.** Formation energy,  $E_f$ , dependencies on the two different inter-edge conformations, which represent bending and rotating forms.

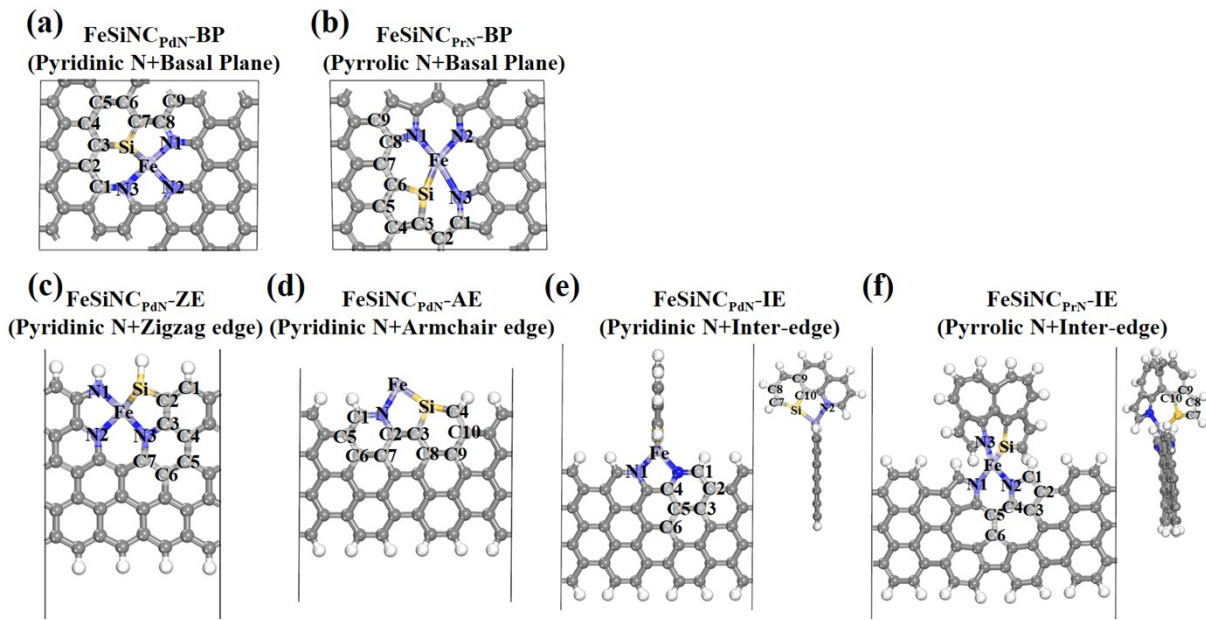


**Fig S15.** Possible Si, Fe and N co-doped graphene structures (FeSiNCs) of (a) FeSiNC<sub>PdN</sub>-BP, (b) FeSiNC<sub>PrN</sub>-BP, (c) FeSiNC<sub>PdN</sub>-ZE, (d) FeSiNC<sub>PdN</sub>-AE, (e) FeSiNC<sub>PdN</sub>-IE and (f) FeSiNC<sub>PrN</sub>-IE (PdN/PrN and BP/AE/ZE/IE represent pyridinic/pyrrolic N and basal plane/armchair/zigzag/inter-edge, respectively).

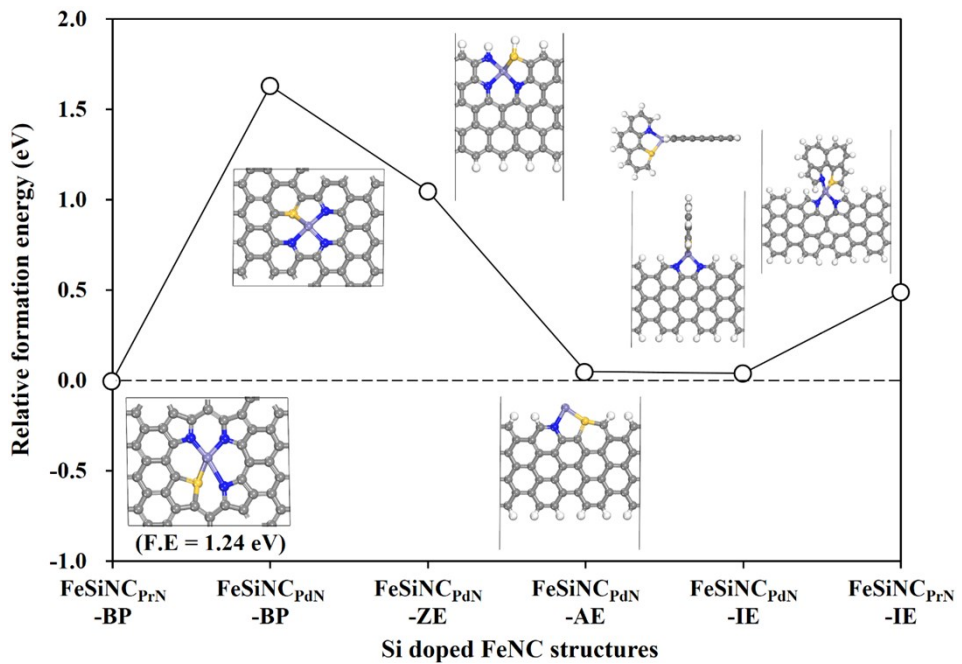


**Fig S16.** Formation energies,  $E_f$ , of Si, Fe and N co-doped graphene structures (FeSiNCs).

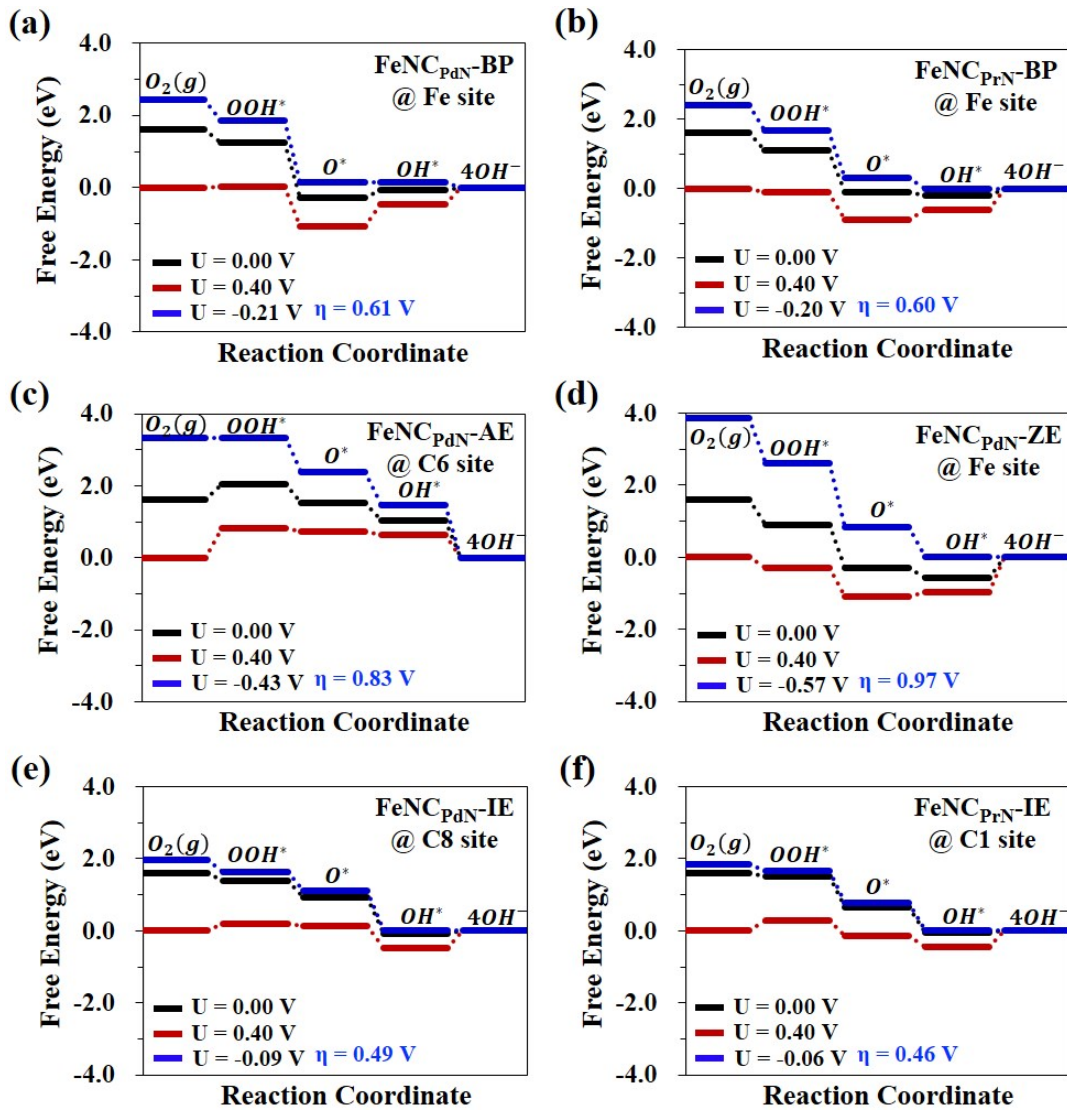


**Fig S17.** ORR Free energy diagrams on (a) FeNC<sub>PdN</sub>-BP, (b) FeNC<sub>PrN</sub>-BP, (c) FeNC<sub>PdN</sub>-ZE, (d) FeNC<sub>PdN</sub>-AE, (e) FeNC<sub>PdN</sub>-IE and (f) FeNC<sub>PrN</sub>-IE in an alkaline environment.

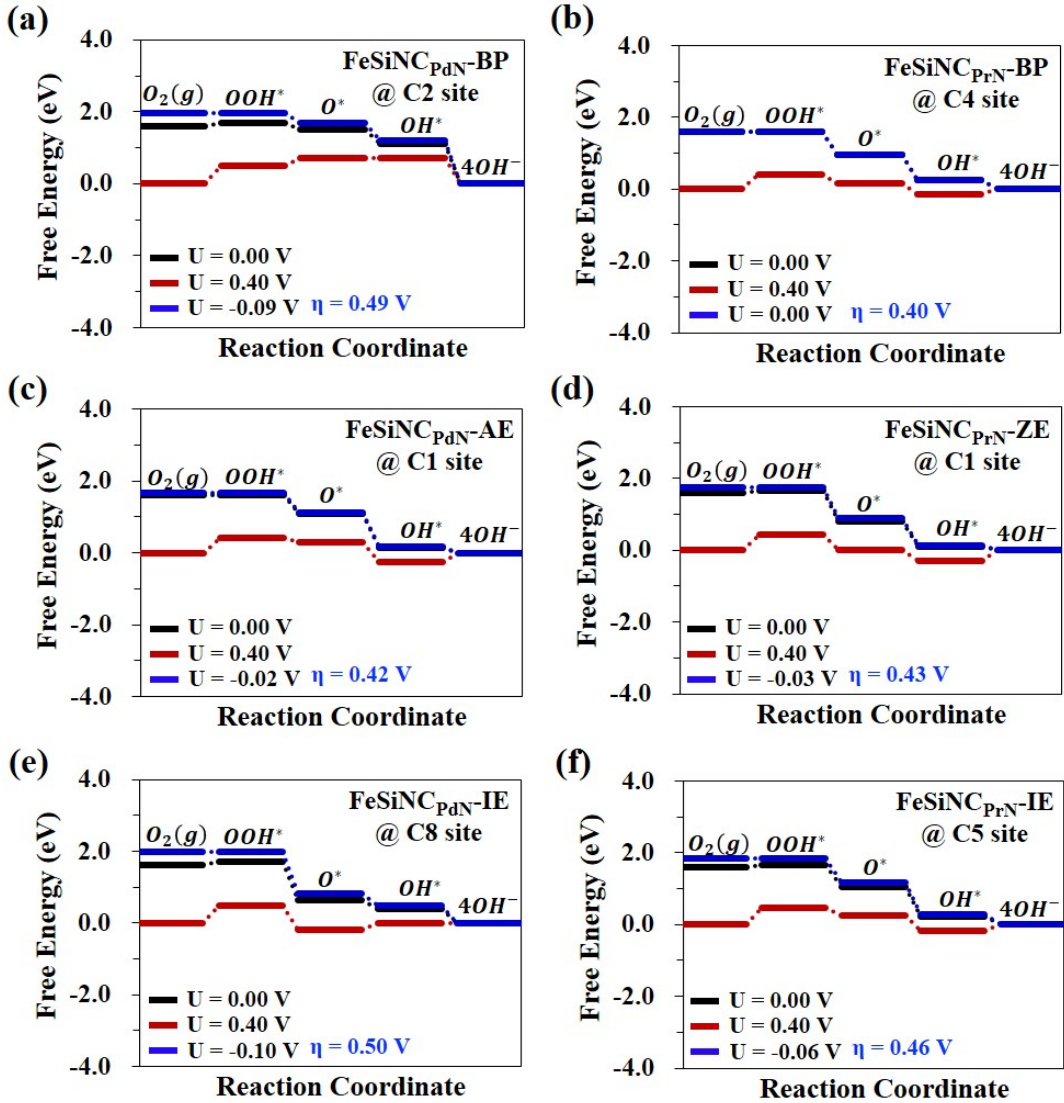


**Fig S18.** ORR Free energy diagrams on (a) FeSiNC<sub>PdN</sub>-BP, (b) FeSiNC<sub>PrN</sub>-BP, (c) FeSiNC<sub>PdN</sub>-ZE, (d) FeSiNC<sub>PdN</sub>-AE, (e) FeSiNC<sub>PdN</sub>-IE and (f) FeSiNC<sub>PrN</sub>-IE in an alkaline environment.

We have performed a detailed analysis for the overpotentials and free energy diagrams (FEDs) under different electrode potentials ( $U=0$  V, 0.402 V and  $\eta$  V), considering four electrons/four pathways (Supporting Information Equation S1-S16). Figs S12 and S13 show FEDs for Fe and N co-doped graphene (FNC) and Si, Fe and N co-doped graphene (SFNC) structures with six different structural configurations, respectively. In the FEDs, we can deduce the  $\eta^{ORR}$ , which is corresponded to the largest endothermic  $\Delta G$  under the standard reaction potential ( $U=0.402$  V in alkaline media), represented by red lines of Fig S12-S13. By applying

$\eta^{O_{RR}}$  to offset the endothermic  $\Delta G$ , we can get the blue lines, in which the calculated results revealed that the FeSiNC<sub>PrN</sub>-BP has the lowest ORR overpotentials of 0.40 V, which represents competitive catalytic activity for conventional Pt.

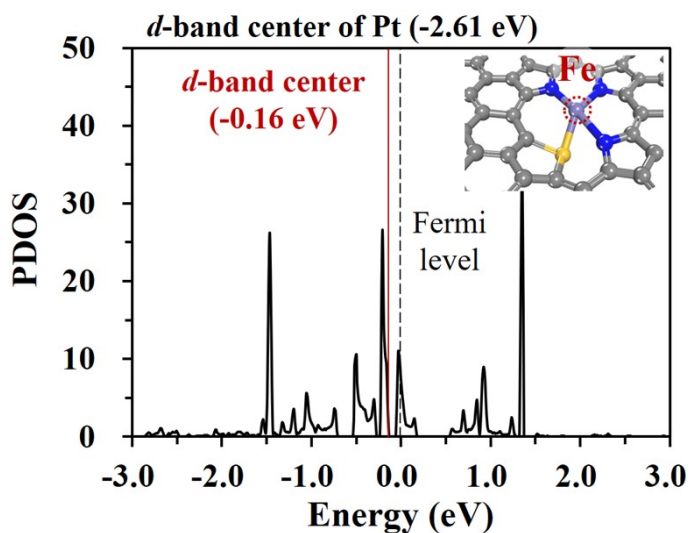


**Fig S19.** Partial density of states (PDOS) of Fe *d*-orbital in FeSiNC<sub>PrN</sub>-BP. The black and red lines represent Fe 3d state and *d*-band center, respectively. The Fermi level is indicated by a black dashed line.

Sample	Elemental	Weight (%)
	C	89.17
	O	8.41
FeSiNC_25a	N	1.68
	Fe	0.55
	Si	0.19
	C	89.01
	O	8.39
FeSiNC_50a	N	1.74
	Fe	0.6
	Si	0.21

**Table S1.** XPS survey results of FeSiNC samples.

<b>Sample</b>	<b>Path*</b>	<b>N</b>	<b>R (Å)</b>	<b><math>\sigma^2</math> (Å<sup>2</sup>)</b>	<b>R-factor (%)</b>
FeSiNC_25a	Fe-N	4.1 ± 1.0	1.960 ± 0.028	0.006 ± 0.003	
	Fe-Si	1.7 ± 0.8	2.430 ± 0.014	0.006 ± 0.004	0.1
	Fe-C	2.5 ± 1.2	3.036 ± 0.034	0.009 ± 0.008	
FeSiNC_50a	Fe-N	4.4 ± 1.7	1.914 ± 0.040	0.008 ± 0.004	
	Fe-Si	3.3 ± 1.7	2.408 ± 0.038	0.008 ± 0.005	0.8
	Fe-C	4.9 ± 2.8	3.014 ± 0.058	0.011 ± 0.008	

**Table S2.** Summary of EXAFS fitting. (N = coordination number, R = interatomic distance,  $\sigma^2$  = Debye-Waller factor (bond disorder), R-Factor = a measure of the quality of EXASFS fit, \* : fixed parameter)

Sample	On-set Potential (v vs RHE)	Half-wave (V vs RHE)	References
Fe-N-CNF	0.93	0.81	Ref. S11.
Fe-NMCs	1.027	0.86	Ref. S12.
Fe@C-FeNC-2	-	0.899	Ref. S13.
Fe-N/C-800	0.923	0.809	Ref. S14.
PMF-800	-	0.861	Ref. S15.
N-CSN-120	0.888	0.754	Ref. S16.
Fe-N-CC	0.94	0.83	Ref. S17.
Fe <sub>3</sub> C/C-800	1.05	0.83	Ref. S18.
CoP NCs	0.8	0.7	Ref. S19.
NPOMC-L1	0.92	0.82	Ref. S20.
Co <sub>3</sub> O <sub>4</sub> /N-rmGo	0.9	0.83	Ref. S21
CoP-CMP800	0.844	0.774	Ref. S22
NL-C	0.95	0.85	Ref. S23
FeSiNC_50a*	1.02*	0.858*	In this work

**Table S3.** Comparison of ORR performances of various samples in published data. (0.1M KOH at 1600 rpm) \*RHE (V) = Ag/AgCl (V) + 0.964V

Sample	Power Density (mW/cm <sup>2</sup> )	References
Maximum		
C-MOF-C2-900	105	Ref. S24
Fe-N-C	100	Ref. S25
NDGs-800	115	Ref. S26
NiCo <sub>2</sub> O <sub>4</sub> @MnO <sub>2</sub> -CNTs-3	86	Ref. S27
CN-800	80	Ref. S28
FeBNC-800	9	Ref. S29
N-HCN	76	Ref. S30
CF-K-A	62	Ref. S31
CNTs@Co-N-C	148	Ref. S32
Co-NCNT/Ng-900	174	Ref. S33
SN-PC-a	11	Ref. S34
N,P-NC-1000	146	Ref. S35
FeSiNC_50a	127	In this work

**Table S4.** Comparison of primary Zn-Air battery performances of various samples in published data.

Sample	Catalyst loading (mg/cm <sup>2</sup> )	Maximum Current density (mA/cm <sup>2</sup> )	Maximum Power density (mW/cm <sup>2</sup> )	Ref
Fe-NMG-35wt%	3.5	670	218	Ref. S36
Fe-N-CC	0.2	375	123	Ref. S37
Pd-N/3D-GN	0.3	910	250	Ref. S38
SNBC12	2.0	810	217	Ref. S39
Fe-N-Co@C-800-AL	3.0	355	137	Ref. S40
Fe/Co-NpGr	2.5	54.4	35	Ref. S41
m-FePhen-C	1.0	830	272	Ref. S42
Fe <sub>0.5</sub> -N-C	1.0	1670	504	Ref. S43
Fe/N/CDC	1.5	230	80	Ref. S44
Fe-LC-900	2.0	360	164	Ref. S45
Co <sub>1.08</sub> Fe <sub>3.34</sub> @NGT	3.0	400	117	Ref. S46
CNT/PC	2.0	1250	380	Ref. S47
Fe-CN-S-800	3.0	450	125	Ref. S48
Co/N/MWCNT	0.6	340	115	Ref. S49
CoMn/pNGr(2:1)	2.0	120	67	Ref. S50
FeCNB-900	2.0	610	172	Ref. S51
FeSiNC_50a	3.0	680	208	In this work

**Table S5.** Comparison of AEMFC performance of various samples in published data.

## References

- S1. G. Kresse and G.;Hafner, J. Phys Rev B 1993, 48, 13115-13118.
- S2. G. Kresse and G.;Hafner, J. Phys Rev B 1994, 49, 14251-14269
- S3. G. Kresse and J. Furthmüller, Comput. Mater. Sci. 1996, 6, 15-50.
- S4. G. Kresse and J. Furthmüller, Phys. Rev. B 1996, 54, 11169.
- S5. J. Wellendorff, K. T. Lundgaard, A. Møgelhøj, V. Petzold, D. D. Landis, J. K. Nørskov and T. Bligaard, K. W. Jacobsen, Phys. Rev. B 2012, 85, 235149.
- S6. Kresse, G and Joubert, D. Phys Rev B 1999, 59, 1758-1775.
- S7. Blöchl PE. Phys Rev B 1994, 50: 17953– 17979.
- S8. J. Rossmeisl, Z. W. Qu, H. Zhu, G. J. Kroes and J. K. Norskov, J. Electroanal. Chem. 2007, 607, 83-89.
- S9. J. K. Nørskov, J. Rossmeisl, A. Logadottir, L. Lindqvist, J. R. Kitchin, T. Bligaard and H. Jonsson, J. Phys. Chem. B 2004, 108, 17886-17892.
- S10. I. C. Man, H.-Y. Su, F. Calle-Vallejo, H. A. Hansen, J. I. Martínez, N. G. Inoglu, J. Kitchin, T. F. Jaramillo and J. K. Nørskov, J. Rossmeisl, ChemCatChem 2011, 3, 1159– 1165.
- S11. Z. Y. Wu, X. X. Xu, B. C. Hu, H. W. Liang, Y. Lin, L. F. Chen and S. H. Yu, Angew. Chem., Int. Ed 2015, 54, 8179-8183
- S12. F. L. Meng, Z. L. Wang, H. X. Zhong, J. Wang, J. M. Yan and X. B. Zhang, Adv. Mater. 2016, 28, 7948-7955
- S13. W. J. Jiang, L. Gu, L. Li, Y. Zhang, X. Zhang, L. J. Zhang, J. Q. Wang, J. S. Hu, Z. Wei and L. J. Wan, J. Am. Chem. Soc. 2016, 138, 3570– 3578.
- S14. L. Lin, Q. Zhu and A.-W. Xu, J. Am. Chem. Soc. 2014, 136, 11027-11033.
- S15. W. Yang, X. Liu, X. Yue, J. Jia and S. Guo, J. Am. Chem. Soc. 2015, 137, 1436-1439.
- S16. H. Yu, L. Shang, T. Bian, R. Shi, G. I. N. Waterhouse, Y. Zhao, C. Zhou, L.-Z. Wu, C.-H. Tung and T. Zhang, Adv. Mater. 2016, 28, 5080– 5086.
- S17. A. Ferrero, K. Preuss, A. Marinovic, A. B. Jorge, N. Mansor, D. J. Brett, A. B. Fuertes, M. Sevilla and M. M. Titirici, ACS Nano 2016, 10, 5922– 5932.
- S18. Y. Hu, J. O. Jensen, W. Zhang, L. N. Cleemann, W. Xing, N. J. Bjerrum and Q. F. Li, Angew. Chem. Int. Ed. 2014, 53, 3675-3679.

- S19. Y. Li, F. Cheng, J. Zhang, Z. Chen, Q. Xu and S. Guo, *Small* 2016, 12, 2839–2845.
- S20. S. Lee, M. Choun, Y. Ye, J. Lee, Y. Mun, E. Kang, J. Hwang, Y. H. Lee, C. H. Shin, S. H. Moon, S. K. Kim, E. Lee and J. Lee, *Angew. Chem. Int. Ed.* 2015, 54, 9230.
- S21. Y. Liang, Y. Li, H. Wang, J. Zhou, J. Wang, T. Regier and H. Dai, *Nat. Mater.* 2011, 10, 780– 786.
- S22. Z. S. Wu, L. Chen, J. Liu, K. Parvez, H. Liang, J. Shu, H. Sachdev, R. Graf, X. Feng and K. Müllen, *Adv. Mater.* 2014, 26, 1450– 1455
- S23. M. Graglia, J. Pampel, T. Hantke, T. P. Fellinger and D. Esposito, *ACS Nano* 2016, 10, 4364-4371.
- S24. M. Zhang, Q. Dai, H. Zheng, M. Chen and L. Dai, *Adv. Mater.* 2018, 30, 1705431
- S25. L. Zhang, J. Xiong, Y.-H. Qin and C.-W. Wang, *Carbon*, 2019, 150, 475–484
- S26. Q. Wang, Y. Ji, Y. Lei, Y. Wang, Y. Wang, Y. Li and S. Wang, *ACS Energy Lett.*, 2018, 3, 1183–1 191
- S27. N.N. Xu, Y.X. Cai, L.W. Peng, J.L. Qiao, Y.D. Wang, W.M. Chirdon and X.D. Zhou, *Nanoscale* 2018, 10, 13626-13637.
- S28. L. Wang, C. Yang, S. Dou, S. Wang, J. Zhang, X. Gao, J. Ma and Y. Yu, *Electrochim. Acta*, 2016, 219, 592–603 .
- S29. K. Yuan, S. Sfaelou, M. Qiu, D. Lützenkirchen-Hecht, X. Zhuang, Y. Chen, C. Yuan, X. Feng and U. Scherf, *ACS Energy Lett.* 2017, 3, 252-260.
- S30. J. Zhu, H. Zhou, C. Zhang, J. Zhang and S. Mu, *Nanoscale*, 2017, 9, 13257–13263 .
- S31. J. Zhu, W. Li, S. Li, J. Zhang, H. Zhou, C. Zhang, J. Zhang and S. Mu, *Small*, 2018, 14, 1800563–1800571
- S32. X. Chen, S. Wang, Y. Wang, Z. Yang, S. Liu, J. Gao, Z. Su, P. Zhu, X. Zhao and G. Wang, *Electrocatalysis* 2019, 10, 277-286.
- S33. K. Fu, Y. Wang, L. Mao, X. Yang, J. Jin, S. Yang and G. Li, *Chem. Eng. J.*, 2018, 351, 94–102 .
- S34. H. L. Lin, D. M. Chen, C. B. Lu, C. Zhang, F. Qiu, S. Han and X. D. Zhuang, *Electrochim. Acta*, 2018, 266, 17-26.
- S35. H. Luo, W.-J. Jiang, Y. Zhang, S. Niu, T. Tang, L.-B. Huang, Y.-Y. Chen, Z. Wei and J.-S. Hu, *Carbon*, 2018, 128, 97–105 .
- S36. M. M. Hossen, K. Artyushkova, P. Atanassov and A. Serov, *J. Power Sources*, 2018, 375, 214–

- S37. G. A. Ferrero, K. Preuss, A. Marinovic, A. B. Jorge, N. Mansor, D. J. Brett, A. B. Fuertes, M. Sevilla and M. M. Titirici, *ACS Nano* 2016, 10, 5922– 5932.
- S38. S. Kabir, A. Serov, K. Artyushkova and P. Atanassov, *ACS Catal.*, 2017, 7, 6609–6618 .
- S39. M. J. Kim, J. E. Park, S. Kim, M. S. Linn, A. Jin, O. H. Kim, M. J. Kim, K. S. Lee, J. Kim, S. S. Kim, Y. H. Cho and Y. E. Sung, *ACS Catal.* 2019, 9, 3389-3398.
- S40. H.-C. Huang, C.-Y. Su, K.-C. Wang, H.-Y. Chen, Y.-C. Chang, Y.-L. Chen, K.C.W. Wu and C.-H. Wang, *ACS Sustainable Chem. Eng.* 2019, 7, 3185-3194.
- S41. T. Palaniselvam, V. Kashyap, S. N. Bhange, J. B. Baek and S. Kurungot, *Adv. Funct. Mater* 2016, 26, 2150-2162.
- S42. Y. Mun, M. J. Kim, S.-A. Park, E. Lee, Y. Ye, S. Lee, Y.-T. Kim, S. Kim, O.-H. Kim and Y.-H. Cho, *Appl. Catal., B*, 2018, 222, 191-199.
- S43. S. H. Lee, J. Kim, D. Y. Chung, J. M. Yoo, H. S. Lee, M. J. Kim, B. S. Mun, S. G. Kwon, Y.-E. Sung and T. Hyeon, *J. Am. Chem. Soc.* 2019, 141, 2035-2045.
- S44. S. Ratso, I. Kruusenberg, M. Käärik, M. Kook, L. Puust, R. Saar, J. Leis and K. Tammeveski, *J. Power Sources* 2018, 375, 233– 243
- S45. R. Soni, S. N. Bhange and S. Kurungot, *Nanoscale* 2019, 11, 7893-7902.
- S46. S. Sultan, N. Tiwari Jitendra, J.-H. Jang, M. Harzandi Ahmad, F. Salehnia, S.J. Yoo and K.S. Kim, *Adv. Energy Mater.* 2018, 8, 1801002.
- S47. Y. J. Sa, D.-J. Seo, J. Woo, J. T. Lim, J. Y. Cheon, S. Y. Yang, J. M. Lee, D. Kang, T. J. Shin and H. S. Shin, *J. Am. Chem. Soc.* 2016, 138, 15046-15056.
- S48. K.-C.Wang, H.-C. Huang, S.-T .Chang, C.-H .Wu, I .Yamanaka, J.-F .Lee and C.-H.Wang,. *ACS Sustainable Chem. Eng.* 2019, 7, 9143–9152
- S49. I. Kruusenberg, D. Ramani, S. Ratso, U. Joost, R. Saar, P. Rauwel, A. M. Kannan and K. Tammeveski, *ChemElectroChem* 2016, 3, 1455– 1465.
- S50. S. K. Singh, V. Kashyap, N. Manna, S. N. Bhange, R. Soni, R. Boukherroub, S. Szunerits and S. Kurungot, *ACS Catal.* 2017, 7, 6700.
- S51. L.-M. Liao, G.-Q. Yu, P.-J. Wei and J.-G. Liu, *ChemElectroChem*, 2019, 6, 1754-1760 .